

## Nonreciprocity and Circulation in a Passive Josephson-Junction Ring

Arkady Fedorov, N. Pradeep Kumar, Dat Thanh Le, Rohit Navarathna, Prasanna Pakkiam, and Thomas M. Stace<sup>1b</sup>

*Analog Quantum Circuits Pty. Ltd., Brisbane, Australia*

*and School of Mathematics and Physics, University of Queensland, Brisbane, QLD 4072, Australia*

 (Received 11 August 2023; revised 30 January 2024; accepted 2 February 2024; published 29 February 2024)

Building large-scale superconducting quantum circuits will require miniaturization and integration of supporting devices including microwave circulators, which are currently bulky, stand-alone components. Here, we report the measurement of microwave scattering from a ring of Josephson junctions, with dc-only control fields. We detect the effect of quasiparticle tunneling, and dynamically classify the system at its operating design point into different quasiparticle sectors. We optimize the device within one of the quasiparticle sectors, where we observe an unambiguous signature of nonreciprocal 3-port scattering within that sector. This enables operation as a circulator, and at the optimal circulation point, we observe on-resonance insertion loss of 2 dB, isolation of 14 dB, power reflectance of  $-11$  dB, and a bandwidth of 200 MHz, averaged over the 3 input ports.

DOI: 10.1103/PhysRevLett.132.097001

Circulators are nonreciprocal multiport devices used to route electromagnetic signals [1], and are ubiquitous in cryogenic microwave circuits [2–4] for isolating a system under test from thermal noise [5,6]. Conventional ferrite microwave circulators are centimeter scale, magnetized units which are not amenable to microfabrication and integration on chip, and thus present a constraint on the development of large-scale solid-state quantum processors. Various approaches to miniaturizing nonreciprocal signal routing have been proposed, including actively driven systems which require additional radio frequency or microwave control fields [5,7–19] and quantum-Hall based devices which require large magnetic fields [20–22].

Here, we report the experimental observation of microwave circulation in a passive, on-chip superconducting device first proposed by Koch *et al.* [23], which consists of three superconducting, tunnel coupled, aluminum islands arranged in a ring topology. This microfabricated, on-chip device is predicted to exhibit high-performance microwave circulation without large magnetic or dynamical control fields [24,25], making it a promising candidate for miniaturizing and integrating microwave circulators with other superconducting devices on the same wafer.

The experimental system is represented in Fig. 1, including the three aluminum islands, indicated by the green, blue, and red boxes, which are deposited on a silicon wafer. The islands are capacitively coupled to one another, to ground, and to the external waveguides through which the system is driven by input signals,  $V_{1,2,3}^{(i)}$ . The scattered output,  $V_{1,2,3}^{(o)}$ , is used to determine the scattering matrix amplitudes,  $S_{ba} = V_b^{(o)}/V_a^{(i)}$ , with  $a, b \in \{1, 2, 3\}$ . The system response depends on the driving frequency, the external flux bias, and the dc charge bias applied to the superconducting islands.

Our previous modeling of this system, based on the open-systems scattering formalism [26], quantizes the nodal flux and charge at each island,  $\hat{\phi}_{1,2,3}$  and  $\hat{n}_{1,2,3}$ , respectively, and constructs a Hamiltonian,  $H_{\text{ring}}$ , which is capacitively coupled to three waveguides [24,25]. Recently, we validated our theoretical model against experimental results in a different device design, establishing good quantitative agreement between theory and experiment [27]. We adopt the same theoretical model to analyze the experimental results reported here. Briefly, the Hamiltonian describing the ring is parametrized by the

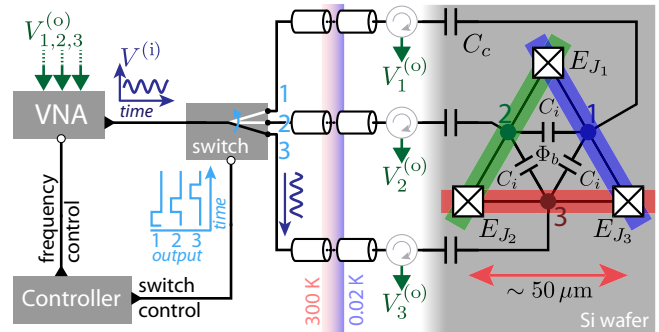


FIG. 1. Circuit diagram for the experimental system. The core device is a ring of three overlapping aluminum islands (green, blue, and red boxes), each  $\sim 50 \mu\text{m}$  long, which are mutually tunnel coupled by junctions with Josephson energies  $E_{J_{1,2,3}}$ . The islands couple capacitively to each other,  $C_i$ , to external waveguides and dc biases,  $C_c$ , and to ground,  $C_g$  (not shown). A controller sets the drive signal  $V^{(i)}$  from a vector network analyzer (VNA), and a fast microwave switch that directs the signal to one of the three waveguide inputs. The scattered signals  $V_{1,2,3}^{(o)}$  are directed back to the VNA.

three Josephson tunnel-junction energies,  $E_{J_{1,2,3}}$ , and the lumped-element capacitance matrix, which includes capacitances between the metallic islands,  $C_i$ , the waveguides and the islands,  $C_c$ , and the island capacitances to ground,  $C_g$ .

For ideal circulation, the ring Hamiltonian should be symmetric under permutations of the node labels, requiring the three islands to be electrically symmetric. This requires the junction energies to be identical, and the system's capacitance matrix to be symmetric. In practice, the electrical symmetry is broken by fabrication variations, for example, leading to a spread in the actual  $E_J$ 's or  $C_i$ 's. Our earlier modeling predicted good circulation when the spread in junction energies was within 1% of the design values [24,25].

The ring device is voltage tunable, so it is sensitive to charge fluctuations. One of the key empirical observations in Navarathna *et al.* [27] was the presence of discrete charge fluctuations that were well described by a ( $K = 4$ )-state hidden Markov model (HMM) with state lifetimes  $\sim 200 \mu\text{s}$ . These HMM states were hypothesized to arise from quasiparticle tunneling between the islands, which generates four distinct quasiparticle sectors, labeled as *eee*, *ooo*, *oeo*, and *ooe* [25]. The reference configuration, *eee* consists of [*e*]ven quasiparticle parity on each island; a quasiparticle-tunneling event changes this to [*O*]dd parity on two of the islands.

To quantify the circulation performance of the device, we define the average clockwise and anticlockwise circulation fidelities, and the average reflection respectively as

$$\mathcal{F}_{\odot} = (|S_{12}| + |S_{23}| + |S_{31}|)/3, \quad (1a)$$

$$\mathcal{F}_{\ominus} = (|S_{13}| + |S_{32}| + |S_{21}|)/3, \quad (1b)$$

$$\mathcal{R} = (|S_{11}| + |S_{22}| + |S_{33}|)/3. \quad (1c)$$

An ideal clockwise circulator will have  $\mathcal{F}_{\odot} = 1$ .

A conservative scattering element is described by a unitary matrix  $S = e^{iG}$ , with Hermitian generator  $G$ . In addition, if the scattering is time-reversal symmetric, then  $G = G^* = G^T$  and  $S$  will be symmetric,  $S = S^T$ . It is straightforward to show that for a time-reversal-symmetric  $3 \times 3$  scattering matrix,  $\mathcal{F} \leq 2/3$ . It follows that a scattering element with  $\mathcal{F} > 2/3$  is an unambiguous signature of time-reversal-symmetry breaking suitable for nonreciprocal scattering.

The results we report here are based on a device that was designed and computationally optimized to have highly symmetric capacitances and Josephson energies. Fabrication was undertaken as in Navarathna *et al.* [27], using electron-beam lithography to pattern the design on a bilayer resist stack. Standard double-angle evaporation was then used to deposit two layers of aluminum, of 20 and 60 nm, respectively, on a high-resistivity silicon substrate, with a single

oxidation step between the two aluminum deposition stages to grow the Josephson tunnel barriers in the device. The different film thicknesses provide a quasiparticle trapping potential. After evaporation, the chip was cleaved and bonded on a holder suitable for cryogenic measurements in a dilution refrigerator operating at a base temperature of 20 mK.

To characterize the system, we first measure the spectral response. Figure 2(a) shows the signal-to-noise ratio (SNR) of the voltage transmission from port 1 to port 2,  $V_{12}$ , as a function of drive frequency, and a flux bias,  $\Phi_b$ , which is provided by a small external coil mounted on the bottom of the sample holder; this could be replaced by an on-chip flux-bias line. The characteristic Y shape of the spectrum has been predicted [24,25] and seen experimentally [27] in our earlier work, as has the multiplets of lines associated to quasiparticle sectors. Ideally, the spectrum should be symmetric under inversion of the flux bias (so that the left and right halves of the spectrum should be reflected), but this symmetry is broken in the data shown: we see a single ‘‘glitch’’ indicated by the arrow, with subtle but distinct variations in the multiplet structure on the left and right of the plot.

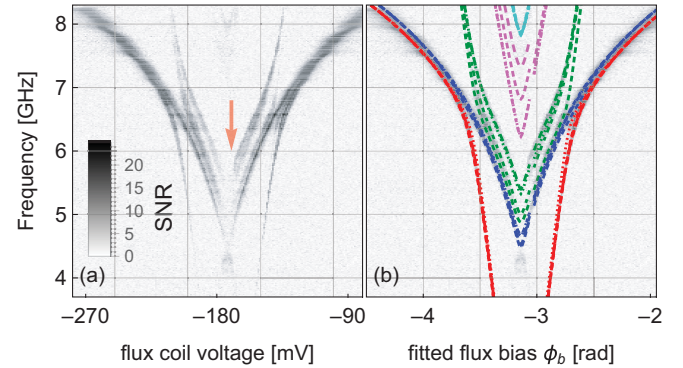


FIG. 2. (a) Measured spectral response of the microwave voltage transmission from port  $a = 1$  to port  $b = 2$ ,  $V_{12}$ , as a function of flux coil voltage. For each frequency, the raw output voltage data are scaled so that the off-resonant background data have zero mean and unit variance; the gray scale therefore represents the output signal-to-noise ratio (SNR). There is a noticeable ‘‘glitch’’ indicated by the arrow, with subtle differences between the left and right halves of the spectrum. (b) Fitted model spectrum superimposed on the measured spectrum, including four distinct quasiparticle sectors. The fitted model includes a linear scale factor and an offset value to convert the flux coil voltage into a dimensionless flux bias  $\phi_b = 2\pi\Phi_b/\Phi_0$ . Different colors correspond to modeled transition frequencies from the ground state to the first excited state (red), second (blue), third (green), fourth (pink), and fifth (aqua); the fourfold multiplicity within the predicted spectrum arises from the different quasiparticle sectors. To account for the glitch in panel (a), we allow for different charge bias configurations on the left and right halves of the modeled spectrum, consistent with a local charge shift that occurred midway through the data collection.

Figure 2(b) shows the spectrum predicted by our theoretical model, fitted to, and superimposed upon, the same SNR data, with the horizontal axis rescaled into units of dimensionless flux bias  $\phi_b = 2\pi\Phi_b/\Phi_0$ , where  $\Phi_0 = h/(2e)$ . The Y shape of the spectrum is centered at  $\phi_b = -\pi$ , as required by theory. It shows the predicted transition frequencies from the ground state to different excited states (colors). The model fitting gives an on-site capacitive energy  $E_{C_\Sigma}/h = (2e)^2/(hC_\Sigma) = 2.97$  GHz, corresponding to a total island capacitance of  $C_\Sigma = C_g + C_c + 3C_i = 52$  fF which is consistent with the designed capacitances ( $C_g = 3.5$  fF,  $C_c = 25$  fF, and  $C_i = 8$  fF) and Josephson energies  $E_{J_{1,2,3}}/h = 11.8, 11.8,$  and  $12.06$  GHz. The spectrum is  $2\pi$  periodic in  $\phi_b$ , which is described in Supplemental Material [28], as are details of the fitting.

The Josephson energy is inversely related to the room-temperature junction resistance,  $E_J \propto 1/R_J$  [29]. We measured  $R_{J_{1,2,3}} = 11.37, 11.35,$  and  $11.16$  k $\Omega$ , respectively, for this device. The spread of 1.9% in  $R_J$ 's is consistent with the 2.2% spread of  $E_J$ 's found above.

The fact that the theoretical spectrum shown in Fig. 2(b) obscures the salient features in the SNR data demonstrates that the model explains the spectral data well. Within each transition band, there are four distinct curves, corresponding to the different quasiparticle sectors. For some transitions (e.g., the red and blue lines), these are nearly degenerate, and in others they are more distinct, but in all cases the underlying multiplets in the data are explained by the theoretical model.

Next, we measure the full  $3 \times 3$  complex scattering matrix. We do this using a fast microwave switch to sequentially direct the drive to each of the three input ports for 100  $\mu$ s, and measure the three output ports with a vector network analyser, as represented in Fig. 1; each sample of  $S$  takes  $\tau_s = 300$   $\mu$ s. We do this for different drive frequencies, bias voltages, and bias currents, to yield a large set of time-series data.

Figure 3(a) shows the imaginary voltage amplitude,  $Q_{23}$  (where  $V_{ba} = I_{ba} + iQ_{ba}$  for transmission from port  $a$  to port  $b$ ), for a time series spanning 3000 samples, at a fixed drive frequency, bias voltage, and flux. We see characteristic jumps between discrete output voltage states [27]. We use a  $K$ -means classifier to separate the discrete voltage states in the time series into  $K = 4$  statistically distinct Gaussian subpopulations, which are depicted in Fig. 3(a) with different colors. Each subpopulation is characterized by a mean and covariance [30], and characteristic dwell times of 9, 11, 12, and 23 samples, i.e., 2.7, 3.2, 3.8, and to 6.7 ms, respectively. This is over ten times longer than the quasiparticle hopping times ( $\sim 200$   $\mu$ s) noted in earlier devices [27], which we attribute to improved infrared shielding and also possibly to a higher  $\bar{E}_J/E_{C_\Sigma}$  ratio to reduce the charge-parity-switching rates [31]. We also show a projection of the subpopulations into the complex

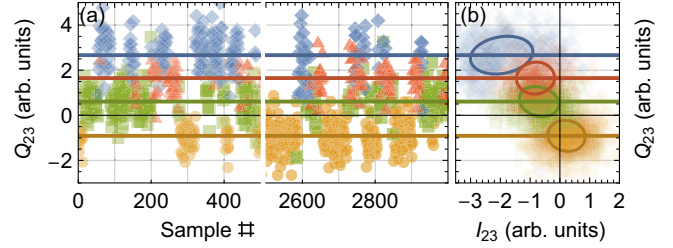


FIG. 3. (a) Leading and trailing subsets of the time series data of the quadrature voltage signal,  $Q_{23}$ , transferred from port  $a = 3$  to port  $b = 2$  for 3000 measurement samples taken with sample measurement time  $\tau_s = 300$   $\mu$ s. The samples are classified into one of  $K = 4$  subpopulations, indicated by point color and shape, using a  $K$ -means classifier, with population means indicated by horizontal lines. We identify the subpopulations with different quasiparticle sectors. (b) Projection of the 3000 complex voltage amplitudes  $V_{23} = I_{23} + iQ_{23}$  classified by sector, together with  $1\sigma$  covariance ellipses centered on each sector mean. The system was tuned to optimize the circulation fidelity in sector 1, corresponding to a flux coil voltage of 214 mV and charge bias voltages of 5, 210, and 6 mV in the three islands, and the drive frequency was 6.8 GHz.

$V_{23}$  plane in Fig. 3(b), together with the projected  $1\sigma$  sample-covariance ellipses for each. [Note that the classifier simultaneously analyses all nine complex-valued voltages  $V_{ba}$ , so that the statistical distance between the populations in this time series is substantially larger than the projection shown in Fig. 3(b).] We attribute these four subpopulations to the four quasiparticle sectors described previously [25,27]. We note that we cannot unambiguously attribute the sectors labeled  $\{1, 2, 3, 4\}$  to specific physical charge configurations  $\{eee, eoo, oeo, ooe\}$ , since we do not have access to the microscopic charge parity of each island; only transitions between different charge-parity configurations are observed.

Next, we fix external bias voltages and fluxes at a working point with high circulation fidelity, and measure scattering data while scanning the drive frequency. We are interested in the scattering at the device, and so we factor out the transfer functions between the VNA and the device; this calibration is described in Supplemental Material [28]. We obtain the spectral response of the device scattering matrix for each of the four sectors, which are shown for sector 1 in Fig. 4(a), and for sector 3 in Fig. 4(b) (scattering spectra for sectors 2 and 4 are similar to sector 3 and are shown in Supplemental Material [28]). The most important comparative feature of the frequency responses is that the measured scattering matrix for sector 1 is strongly asymmetric,  $S \neq S^T$  (e.g., around 6.8 GHz,  $|S_{12}| > |S_{21}|$ ,  $|S_{23}| > |S_{32}|$ , and  $|S_{31}| > |S_{13}|$ ), whereas the scattering matrix for sector 3 is approximately symmetric,  $S \approx S^T$ . The scattering asymmetry in Fig. 4(a) shows that the device circulates when it is in the state corresponding to sector 1, while Fig. 4(b) shows that it does not circulate in the other sectors, consistent with the quasiparticle analysis in Le *et al.* [25].

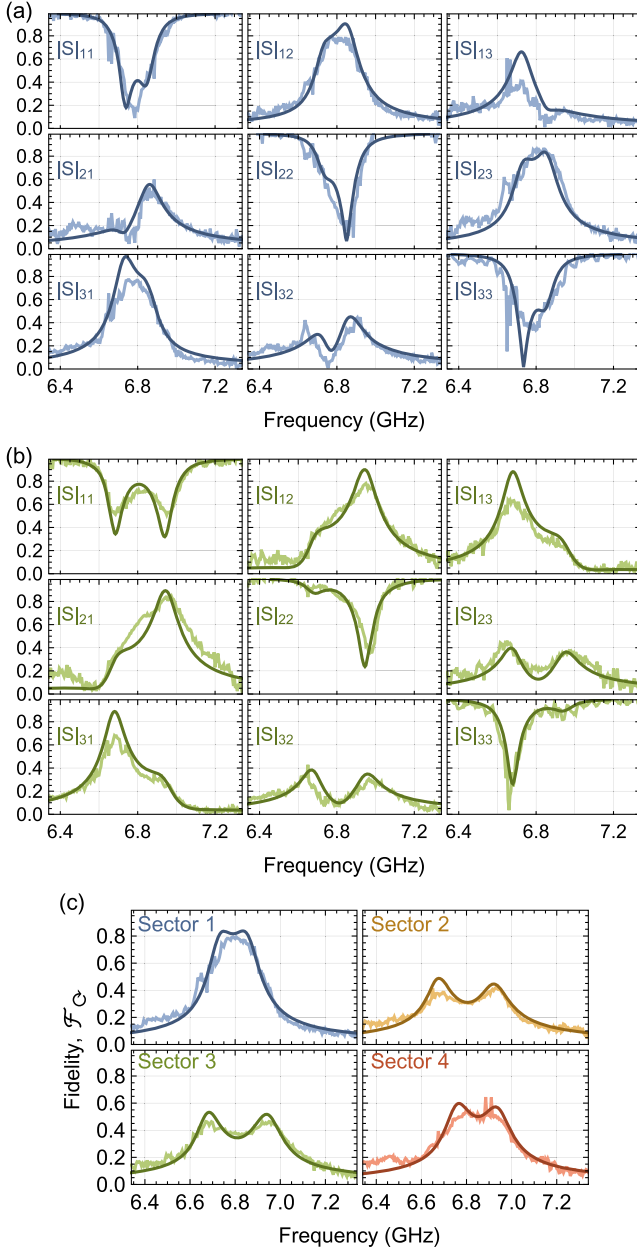


FIG. 4. (a) Scattering matrix elements  $|S|_{ba}$  for time-series data classified as sector 1, which shows strong asymmetry in the scattering matrix,  $S \neq S^T$ , near 6.8 GHz. (b) Scattering matrix elements for sector 3, which is quite symmetric for all frequencies,  $S \approx S^T$ . Experimental data (light) shows good agreement with model calculations (dark). Scattering matrix spectra for sectors 2 and 4 look qualitatively similar to (b). (c) The clockwise circulation fidelity,  $\mathcal{F}_C$ , of scattering matrices in each sector, showing experimental data and model predictions. The system was tuned to the same flux and bias voltages, and with the sectors indicated by the same color scheme as in Fig. 3.

Figure 4 also shows model predictions (darker curves), using the same circuit parameters used to generate the spectra in Fig. 2(b), with a fitted coupling strength at  $\kappa = 119$  MHz for each waveguide. The only model parameter

we vary between the theory curves in Figs. 4(a) and 4(b) is the offset charge bias on two of the islands, consistent with a discrete change in charge state due to quasiparticles in these two sectors. We see good agreement between the data and the model predictions, with resonance frequencies and strengths reasonably well matched in each sector.

We compare circulation in the four sectors using the circulation fidelity measure  $\mathcal{F}_C$ , shown in Fig. 4(c). We see high fidelity clockwise circulation in sector 1, reaching  $\max \mathcal{F}_C = 0.8$ , well above the  $\mathcal{F} \leq 2/3$  bound for time-reversal symmetric devices, and with a bandwidth of 200 MHz at full width at half maximum; this is consistent with the prediction in Ref. [25] [see Eq. (11) therein]. Conversely, the other sectors have maximum fidelities lower than the time-reversal-symmetric threshold, and do not show strong circulation. In all sectors, the circulation fidelity inferred from the measurements is in good agreement with the model using parameters obtained from the spectral fitting. The consistency between the modeling and experimental data indicate that the observed circulation is limited by the  $\sim 2\%$  variation in the junction energies,  $E_{J_{1,2,3}}$ .

We are able to tune the device operation by application of dc voltage and flux biases. These enable us to dynamically reverse the direction of circulation, which we have observed in this device. The performance for anticlockwise circulation is similar to that in the clockwise tuning, shown in Supplemental Material [28].

Finally, we characterize the device performance as a (clockwise) circulator. From the scattering matrix and the quantities defined in Eq. (1), we define the average insertion loss  $IL = \mathcal{F}_C^2$ , the average isolation  $IS = \mathcal{F}_C^2$ , and the average power reflectance  $R = \mathcal{R}^2$ . We plot these in Fig. 5, and see that at the 6.8 GHz resonance frequency,  $IL = 2$  dB,  $IS = 14$  dB and  $R = -11$  dB. In Fig. 5  $IL$  varies by  $< 1$  dB over a bandwidth of 150 MHz, while the average isolation is  $> 14$  dB over a bandwidth of 50 MHz. It thus exhibits a narrower insertion loss bandwidth and a similar isolation bandwidth relative to parametrically driven Josephson devices [12,32]. Other studies [7,11,13,14,18,19,22] showed better isolation, but with bandwidth less than 40 MHz.

The device saturation power will roughly correspond to the arrival of one drive photon per excited-state lifetime,  $\tau_e = (\kappa |\langle e | \hat{n}_a | g \rangle|^2)^{-1}$ , where we use the model to compute  $|\langle e | \hat{n}_a | g \rangle|^2 = 0.38$ , based on fitted device parameters. This estimate gives  $P_{\text{sat}} \approx hf / \tau_e = -127$  dBm, which is smaller than the values reported in parametric devices [11,18,19,32]. This estimate matches with the 3 dB point of numerical simulations, and experimental measurements described in Supplemental Material [28]. Pathways to increasing the saturation power include enhancing the coupling capacitance, better impedance matching, and device multiplexing.

The results presented here improve upon our previous work [27], specifically in the electronic symmetry of the device and quasiparticle lifetimes, resulting in observation

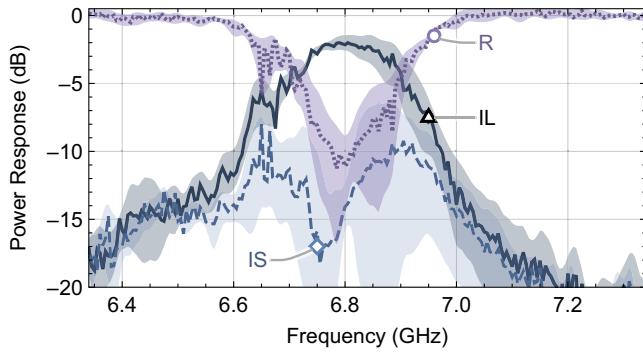


FIG. 5. Average power-transfer matrix-elements for sector 1 data, showing the average insertion loss  $IL = \mathcal{F}_C^2$ , isolation  $IS = \mathcal{F}_D^2$ , and power reflectance  $R = \mathcal{R}^2$ . The shaded region around each quantity indicates its range, estimated from the smoothed maxima and minima over each of the terms in the corresponding sums in Eq. (1).

of unambiguous nonreciprocity and circulation in the relevant quasiparticle sector. In particular, resolving the fast ( $\sim 200 \mu\text{s}$ ) quasiparticle transitions in [27] required fast sample averaging and correspondingly large input powers which partially saturated the device; it also meant that at low power, we could only measure quasiparticle-averaged unsaturated scattering matrices. The  $> 10\times$  longer quasiparticle lifetimes reported here enable longer sample averaging ( $\tau_s = 300 \mu\text{s}$ ) of unsaturated scattering for each HMM state, allowing us to resolve separate quasiparticle sectors in the unsaturated scattering matrices, and then to characterize and optimize the circulation within a quasiparticle sector. However, quasiparticle fluctuations remain a challenge for making practically useful superconducting quantum devices. This is an issue in a wide range of devices, and recent advances in gap engineering [33–35] show quasiparticle lifetimes  $> 1000 \text{ s}$ .

To conclude, we have built a dc-controlled microwave circulator using a ring of tunnel-coupled superconducting islands driven through external waveguides. We observe discrete charge jumps that we classify as quasiparticle tunnelling events through the junctions. When the system response is postselected in the optimized quasiparticle sector we observe strong circulation in the microwave scattering matrix, with unambiguous evidence of time-reversal symmetry breaking. Our measured results are in good quantitative agreement with model predictions, which provides directions to improve performance.

This work was funded through a commercial research contract with Analog Quantum Circuits (AQC) Pty. Ltd. The authors acknowledge assistance from the Centre for Microscopy and Microanalysis at the University of Queensland, and the Australian National Fabrication Facility, ANFF-Q.

T.M.S. and A.K. each declare a financial interest in AQC.

- [1] A. Kord, D. L. Sounas, and A. Alù, *IEEE Trans. Microwave Theory Tech.* **66**, 911 (2018).
- [2] D. Pozar, *Microwave Engineering* (Wiley, New York, 2011).
- [3] X. Gu, A. F. Kockum, A. Miranowicz, Y. xi Liu, and F. Nori, *Phys. Rep.* **718–719**, 1 (2017).
- [4] Y.-Y. Wang, S. van Geldern, T. Connolly, Y.-X. Wang, A. Shilcuskys, A. McDonald, A. A. Clerk, and C. Wang, *Phys. Rev. Appl.* **16**, 064066 (2021).
- [5] A. Metelmann and A. A. Clerk, *Phys. Rev. X* **5**, 021025 (2015).
- [6] F. Ruesink, M.-A. Miri, A. Alù, and E. Verhagen, *Nat. Commun.* **7**, 13662 (2016).
- [7] B. J. Chapman, E. I. Rosenthal, J. Kerckhoff, B. A. Moores, L. R. Vale, J. A. B. Mates, G. C. Hilton, K. Lalumière, A. Blais, and K. W. Lehnert, *Phys. Rev. X* **7**, 041043 (2017).
- [8] A. Kamal, J. Clarke, and M. H. Devoret, *Nat. Phys.* **7**, 311 (2011).
- [9] A. Kamal and A. Metelmann, *Phys. Rev. Appl.* **7**, 034031 (2017).
- [10] N. A. Estep, D. L. Sounas, J. Soric, and A. Alù, *Nat. Phys.* **10**, 923 (2014).
- [11] K. M. Sliwa, M. Hatridge, A. Narla, S. Shankar, L. Frunzio, R. J. Schoelkopf, and M. H. Devoret, *Phys. Rev. X* **5**, 041020 (2015).
- [12] F. Lecocq, L. Ranzani, G. A. Peterson, K. Cicak, R. W. Simmonds, J. D. Teufel, and J. Aumentado, *Phys. Rev. Appl.* **7**, 024028 (2017).
- [13] K. Fang, J. Luo, A. Metelmann, M. H. Matheny, F. Marquardt, A. A. Clerk, and O. Painter, *Nat. Phys.* **13**, 465 (2017).
- [14] C. W. Peterson, W. A. Benalcazar, M. Lin, T. L. Hughes, and G. Bahl, *Phys. Rev. Lett.* **123**, 063901 (2019).
- [15] J. Kerckhoff, K. Lalumière, B. J. Chapman, A. Blais, and K. W. Lehnert, *Phys. Rev. Appl.* **4**, 034002 (2015).
- [16] P. Roushan *et al.*, *Nat. Phys.* **13**, 146 (2017).
- [17] E. I. Rosenthal, B. J. Chapman, A. P. Higginbotham, J. Kerckhoff, and K. W. Lehnert, *Phys. Rev. Lett.* **119**, 147703 (2017).
- [18] B. Abdo, N. T. Bronn, O. Jinka, S. Olivadese, A. D. Córcoles, V. P. Adiga, M. Brink, R. E. Lake, X. Wu, D. P. Pappas *et al.*, *Nat. Commun.* **10**, 3154 (2019).
- [19] B. Abdo, O. Jinka, N. T. Bronn, S. Olivadese, and M. Brink, *PRX Quantum* **2**, 040360 (2021).
- [20] T. M. Stace, C. H. W. Barnes, and G. J. Milburn, *Phys. Rev. Lett.* **93**, 126804 (2004).
- [21] G. Viola and D. P. DiVincenzo, *Phys. Rev. X* **4**, 021019 (2014).
- [22] A. C. Mahoney, J. I. Colless, S. J. Pauka, J. M. Hornibrook, J. D. Watson, G. C. Gardner, M. J. Manfra, A. C. Doherty, and D. J. Reilly, *Phys. Rev. X* **7**, 011007 (2017).
- [23] J. Koch, A. A. Houck, K. L. Hur, and S. M. Girvin, *Phys. Rev. A* **82**, 043811 (2010).
- [24] C. Müller, S. Guan, N. Vogt, J. H. Cole, and T. M. Stace, *Phys. Rev. Lett.* **120**, 213602 (2018).
- [25] D. T. Le, C. Müller, R. Navarathna, A. Fedorov, and T. M. Stace, *Phys. Rev. Res.* **3**, 043211 (2021).

- [26] J. Combes, J. Kerckhoff, and M. Sarovar, *Adv. Phys.* **2**, 784 (2017).
- [27] R. Navarathna, D. T. Le, A. R. Hamann, H. D. Nguyen, T. M. Stace, and A. Fedorov, *Phys. Rev. Lett.* **130**, 037001 (2023).
- [28] See Supplemental Material at <http://link.aps.org/supplemental/10.1103/PhysRevLett.132.097001> for more details on the analysis and results presented in this Letter.
- [29] V. Ambegaokar and A. Baratoff, *Phys. Rev. Lett.* **10**, 486 (1963).
- [30] J. Schreiber, *J. Mach. Learn. Res.* **18**, 1 (2018).
- [31] G. Catelani, J. Koch, L. Frunzio, R. J. Schoelkopf, M. H. Devoret, and L. I. Glazman, *Phys. Rev. Lett.* **106**, 077002 (2011).
- [32] R. Kwende, T. White, and O. Naaman, *Appl. Phys. Lett.* **122**, 224001 (2023).
- [33] J. M. Martinis, *npj Quantum Inf.* **7**, 90 (2021).
- [34] S. Diamond, V. Fatemi, M. Hays, H. Nho, P. D. Kurilovich, T. Connolly, V. R. Joshi, K. Serniak, L. Frunzio, L. I. Glazman, and M. H. Devoret, *PRX Quantum* **3**, 040304 (2022).
- [35] P. Kamenov, T. DiNapoli, M. Gershenson, and S. Chakram, [arXiv:2309.02655](https://arxiv.org/abs/2309.02655).